RSC Advances

PAPER

View Article Online
View Journal | View Issue

Cite this: *RSC Adv.*, 2018, **8**, 42438

3D plum candy-like $NiCoMnO_4$@graphene as anodes for high-performance lithium-ion batteries

Jianming Tao,[abc] Guozhen Liu,[ab] Yuhan Chen,[ab] Yubin Chi,[ab] Lixun Hong,[ab] Zhiya Lin,[ab] Yingbin Lin *[abc] and Zhigao Huang [abc]

Received 25th October 2018
Accepted 27th November 2018

DOI: 10.1039/c8ra08869a

rsc.li/rsc-advances

3D plum candy-like $NiCoMnO_4$ microspheres have been prepared *via* ultrasonic spraying and subsequently wrapped by graphene through electrostatic self-assembly. The as-prepared $NiCoMnO_4$ powders show hollow structures and $NiCoMnO_4$@graphene exhibits excellent electrochemical performances in terms of rate performance and cycling stability, achieving a high reversible capacity of 844.6 mA h g^{-1} at a current density of 2000 mA g^{-1}. After 50 cycles at 1000 mA g^{-1}, $NiCoMnO_4$@graphene delivers a reversible capacity of 1045.1 mA h g^{-1} while the pristine $NiCoMnO_4$ only has a capacity of 143.4 mA h g^{-1}. The hierarchical porous structure helps to facilitate electron transfer and Li-ion kinetic diffusion by shortening the Li-ion diffusion length, accommodating the mechanical stress and volume change during the Li-ion insertion/extraction processes. Analysis from the electrochemical performances reveals that the enhanced performances could be also attributed to the reduced charge-transfer resistance and enhanced Li-ion diffusion kinetics because of the graphene-coating. Moreover, Schottky electric field, due to the difference in work function between graphene and $NiCoMnO_4$, might be favorable for the redox activity of the $NiCoMnO_4$. In light of the excellent electrochemical performance and simple preparation, we believe that 3D plum candy-like $NiCoMnO_4$@graphene composites are expected to be applied as a promising anode materials for high-performance lithium ion batteries.

1. Introduction

In recent years, rechargeable lithium-ion batteries with high energy and power densities have attracted increasing interest due to their commercial application in portable electronic devices, electric vehicles and large-scale energy storage.[1–3] Unfortunately, the commercial graphite anode with low theoretical specific capacity of 372 mA h g^{-1}, could not satisfy the ever-growing demand for high energy-density lithium-ion batteries.[4] Therefore, many strategies have been carried out to develop alternative anode materials with high energy, long cycling life and good rate capability as well.[5,6] Among the explored systems, transition metal oxides have been reinvestigated as the most promising anode materials because of their high capacity, environmental friendliness, widespread availability and abundant oxidation states available for reversible redox reactions.[7–10] In numerous transition metal oxides, spinel cobalt–nickel oxide ($NiCo_2O_4$) have received considerable attention owing to its high specific capacity (~890 mA h g^{-1}), environmental benignity and good electronic conductivity.[11,12] However, $NiCo_2O_4$ suffers from large volume expansion/contraction, electrode pulverization and severe particle aggregation, resulting in loss of particle contact and poor cycling stability during the Li-ion insertion/extraction processes.[13–15] Up to now, lots of effective strategies have been devoted to overcome these shortcomings, such as fabricating hierarchically structure, coupling with conducting substances and doping with isovalent ions.[16–19] Chen *et al.*[16] reported that TiO_2-coating could improve electrochemical performances of flower-like $NiCo_2O_4$ nanosheets, resulting from enhanced structural stability, reduced charge-transfer resistance and improved Li-ion diffusion. Mo *et al.*[17] reported that porous $NiCo_2O_4$@-amorphous carbon delivered a high reversible capacity of 1224.8 mA h g^{-1} at a current density of 500 mA g^{-1}.

In this work, 3D plum candy-like $NiCoMnO_4$@graphene composites have been successfully prepared based on ultrasonic spraying and electrostatic self-assembly method. The partial substitution of Co by Mn can effectively reduce the cost and toxicity of $NiCo_2O_4$ without sacrifice of specific capacity. In addition, plum candy-like and hollow structure obtained with a help of vacuum technique would shorten the Li-ion diffusion length, accommodate the mechanical stress–strain of the active materials during the electrochemical reaction. Moreover, the graphene-wrapping with $NiCoMnO_4$ through electrostatic self-assembly could not only efficiently suppress electrode

[a]*College of Physics and Energy, Fujian Normal University, Fujian Provincial Key Laboratory of Quantum Manipulation and New Energy Materials, Fuzhou, 350117, China. E-mail: yblin@fjnu.edu.cn; Fax: +86-591-2286-8132; Tel: +86-591-2286-8132*

[b]*Fujian Provincial Engineering Technology Research Center of Solar Energy Conversion and Energy Storage, Fuzhou, 350117, China*

[c]*Fujian Provincial Collaborative Innovation Center for Optoelectronic Semiconductors and Efficient Devices, Xiamen, 361005, China*

pulverization and particle aggregation, but also provide a high-conductive network for electron-transfer in the electrode. Owing to the hollow plum candy-like structure and high-conductive graphene network, the as-prepared $NiCoMnO_4$@graphene as a novel anode material for lithium ion batteries exhibits an excellent electrochemical performances in term of rate capability and cycling stability.

2. Experimental section

2.1 Synthesis of $NiCoMnO_4$ microspheres

$NiCoMnO_4$ microspheres are prepared by ultrasonic spraying under the help of vacuum pump, shown in Fig. 1(a and b). Typically, 0.01 mol $Ni(CH_3COO)_2 \cdot 4H_2O$, 0.01 mol $Co(CH_3COO)_2 \cdot 4H_2O$ and 0.01 mol $Mn(CH_3COO)_2 \cdot 4H_2O$ are thoroughly dissolved in 100 mL deionized water, followed by continuous stirring until a pink solution is formed. Then, 0.2 g polyvinyl pyrrolidone (M_w = 58 000) is added to the above aqueous solution under stirring. After vigorous stirring for another 30 min, the resulted solution is ultrasonically atomized and the droplets go through a reactor of 600 °C under the help of vacuum pump. The vacuum atmosphere in the reactor is favorable for the formation of the hollow structure. The Ni–Co–Mn–O precursors are collected and subsequently calcinated at 500 °C for 5 h in air to obtain $NiCoMnO_4$ powders.

2.2 Preparation of $NiCoMnO_4$@graphene composites

$NiCoMnO_4$@graphene composites are prepared by electrostatic interactions between positively charged $NiCoMnO_4$ particles and negatively charged graphene oxide sheets in aqueous solution. Typically, 0.5 g of as-prepared $NiCoMnO_4$ microspheres are dispersed in 50 mL of ethanol under ultrasonication for 30 min, followed by adding 5 mL of 3-aminopropyltriethoxysilane (APTES) under continuous stirring. After vigorous stirring for 5 h, the obtained precipitates are collected by centrifugation and washed with ethanol several times to get amino-silane modified $NiCoMnO_4$ nanoparticles. Then, 0.12 g of amino-silane modified $NiCoMnO_4$ powders are dispersed in 200 mL 0.4 mg mL^{-1} graphite oxide ethanol solution under vigorous sonication for 3 h, in which the positively-charged $NiCoMnO_4$ nanoparticles are strongly adsorbed to the negatively-charged graphene-oxide *via* electrostatic interactions. Finally, the obtained precipitates are collected by centrifugation, washed with de-ionized water several times and consequently calcinated at 300 °C in an Ar atmosphere for 5 h to obtain the final product. The schematic illustration of the synthesis process for $NiCoMnO_4$@graphene is shown in Fig. 1(b).

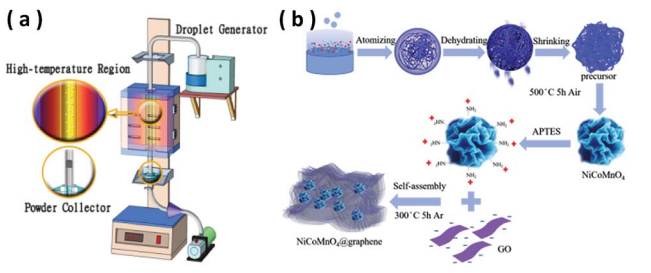

Fig. 1 (a)Schematic diagram of the ultrasonic spraying process. (b) Schematic of the formation process of $NiCoMnO_4$ and $NiCoMnO_4$@graphene.

2.3 Materials characterization

The crystalline structures of the as-prepared composites are characterized by X-ray diffraction (XRD, Rigaku MiniFlex II) using CuK_α radiation (λ = 0.15405 nm). The surface morphologies of the $NiCoMnO_4$ and $NiCoMnO_4$@graphene are determined by a field-emission scanning electron microscopy (FESEM; HITACHI, SU-8010) equipped with an energy-dispersive spectroscopy (EDS). The microstructure of $NiCoMnO_4$ is further examined by on a Tecnai G2 F20 S-Twin high resolution transmission electron microscopy. The chemical state and composition are analyzed using X-ray photoelectron spectroscopy (Thermo Scientific ESCALAB 250Xi). Nitrogen adsorption–desorption isotherms are measured at 77 K on a Micromeritics Tristar 3020 analyzer. The specific surface areas are calculated according to the Brunauer–Emmett–Teller method and the pore size distribution is determined based on Barrett Joyner and Halenda model. Thermogravimetric analysis (TGA) of $NiCoMnO_4$@graphene are conducted on a Netzsch STA449F3 analyzer at a heating rate of 5 °C min^{-1} under an air flow.

2.4 Electrochemical measurements

The electrochemical performances are evaluated by usingCR2025 coin-type cell. The working electrode is prepared by mixing the active material ($NiCoMnO_4$ or $NiCoMnO_4$@graphene), Super-P, and poly(vinylidene fluoride), with a weight ratio of 70 : 20 : 10 in *N*-methyl pyrrolidinone (NMP). The homogeneous slurry is cast onto copper current collector and subsequently dried at 120 °C in vacuum overnight. The obtained laminate is punched into a 12 mm diameter disc and the loading density of the active materials is 1.0–1.2 mg cm^{-2}. Electrochemical cells are assembled in an Ar-filled glove box (O_2 < 0.1 ppm, H_2O < 0.1 ppm) using a Celgard 2400 microporous polypropylene membrane as the separator and lithium foil as the negative electrode. The electrolyte is a solution of 1 M $LiPF_6$ in dimethyl carbonate (DMC)–ethylene carbonate (EC)–diethyl carbonate (DEC) (1 : 1 : 1 in volume). The galvanostatic charge/discharge measurements are carried out on a LAND test system (LAND CT2001A) in a voltage range from 0.01 to 3.0 V. Cyclic voltammogram (CV) and electrochemical impedance spectra (EIS) measurements of the cells are performed on a Zahner Zennium IM6 electrochemical workstation.

3. Results and discussion

3.1 Morphological and physical characterization

Fig. 2(a) shows the typical SEM images of the as-prepared $NiCoMnO_4$ powders. As can be seen, the morphologies of the as-synthesized $NiCoMnO_4$ powders are shriveled microspherical in shape with uniform size of 500–1500 nm, which

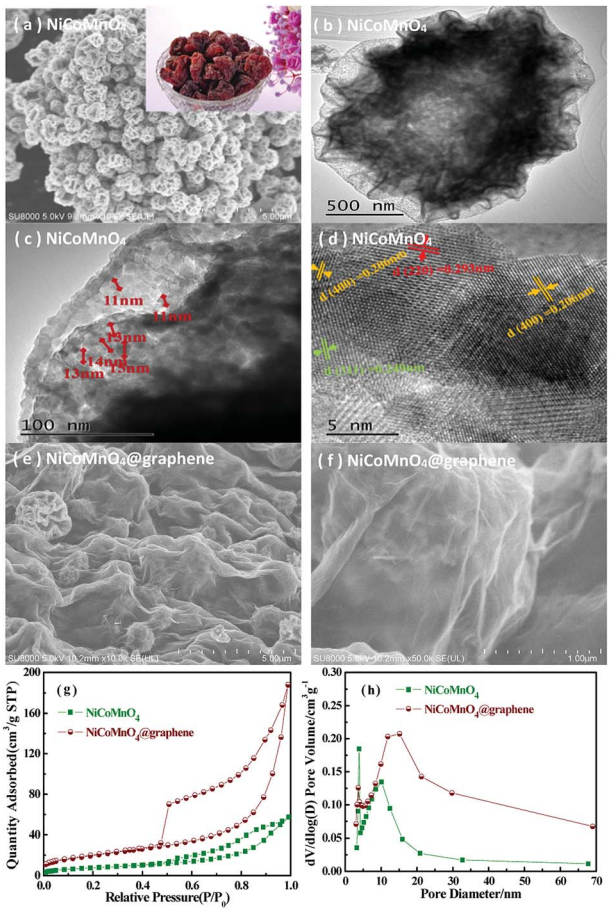

Fig. 2 (a) FE-SEM and (b–d) TEM images of as-prepared $NiCoMnO_4$. (e and f) FE-SEM images of as-prepared $NiCoMnO_4$@graphene. (g) Nitrogen sorption isotherms and (h) pore diameter distribution of $NiCoMnO_4$ and $NiCoMnO_4$@graphene powders.

demonstrate three-dimensional plum candy-like structures. The contrast between the dark edge and the gray center of microsphere shown in Fig. 2(b), revealing the hollow nature of the as-prepared $NiCoMnO_4$ powders. Fig. 2(c) reveals that plum candy-like $NiCoMnO_4$ particle consists of numerous tiny well-crystalline particles with an average particle-size of ~13 nm. Analysis from high-resolution TEM images (Fig. 2(d)) reveals that the distinct lattice fringes with average distance of 0.293, 0.249 and 0.206 nm correspond to the (220), (311) and (400) planes of spinel $NiCoMnO_4$, respectively. Such hierarchical structure would provide plenty of channels for electrolyte permeation and shorten Li-ion diffusion length. The SEM images of $NiCoMnO_4$@graphene powders shown in Fig. 2(e and f), show that $NiCoMnO_4$ particles are wrapped by gauze-like graphene nanosheets and the isolated $NiCoMnO_4$ particles are connected by wrinkled graphene sheets, which provides a high-conductive network for electron-transfer in composites. Fig. 2(g) shows N_2 adsorption/desorption isotherms of the $NiCoMnO_4$ and $NiCoMnO_4$@graphene. Both samples exhibit typical type-IV isotherm curves with obvious hysteresis loops, suggesting a typical characteristic of mesoporous structure for the as-prepared samples.[17,20] Based on Brunauer–Emmett–Teller (BET) theory, the specific surface areas of $NiCoMnO_4$ and $NiCoMnO_4$@graphene are calculated to be 28.01 and 71.60 $m^2 g^{-1}$, respectively. Fig. 2(h) shows Barrett–Joyner–Halenda (BJH) pore-size distribution of $NiCoMnO_4$ and $NiCoMnO_4$@graphene, indicating that $NiCoMnO_4$@graphene has larger average pore size (16.19 nm) than that (12.59 nm) of the pristine one.

The XPS measurements are performed to investigate the chemical state of $NiCoMnO_4$@graphene powders. The survey spectrum (Fig. 3(a)) obviously shows the presence of Ni, Co, Mn, O and C elements in the $NiCoMnO_4$@graphene powders. All XPS signals are fitted with mixed Lorentzian–Gaussian curves. Fig. 3(b) shows that the Ni 2p core-level spectrum has two spin–orbit doublets around 855.1 and 872.8 eV respectively accompanied by two shake-up satellites, which are consistent with the characteristic of Ni^{2+} and Ni^{3+}.[21] Two fitted peaks are observed at 780.6 and 796.0 eV shown in Fig. 3(c) are assigned to Co $2p_{3/2}$ and Co $2p_{1/2}$ spin–orbit doublets, revealing the presence of Co^{2+} and Co^{3+}. Fig. 3(d) presents the Mn 2p core-level spectrum, confirming the existence of Mn^{2+} and Mn^{3+} in composites. Based on the peak area of Ni-2p, Co-2p, Mn-2p, the atomic ratio of Ni, Co and Mn is about 1.03 : 0.96 : 1. The high-resolution O 1s spectrum (Fig. 2(e)) can be divided into three oxygen contributions. The fitting peak located at 529.9 eV is typical of metal–oxygen bonds.[22] The fitting peak located at 531.6 eV is typically related with defects, and under-coordinated lattice oxygen.[23] The fitting peak around 533.0 eV is attributed to surface-absorbed oxygen at or near the surface.[24] The high-resolution C 1s spectrum (Fig. 2(f)) reveals many functional groups such as C–C/C–C (284.9 eV), C–OH (286.2 eV) and C–O (288.7 eV) on the graphene sheets, which are greatly association with $NiCoMnO_4$ by covalent chemical bond, hydrogen bonding

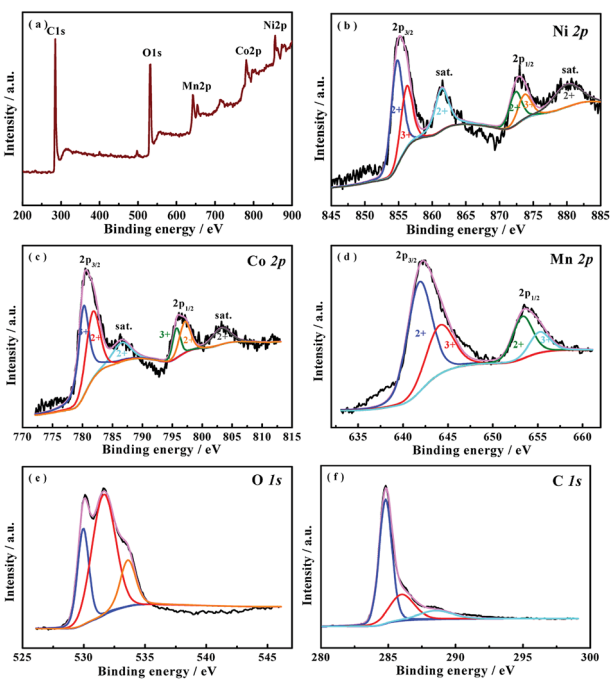

Fig. 3 XPS spectra of (a) survey spectrum, (b) Ni 2p, (c) Co 2p, (d) Mn 2p and (e) O 1s (f) C 1s for the $NiCoMnO_4$@graphene powders.

or van der Waal's forces, and favor direct growth of $NiCoMnO_4$ on rGO sheets.[25] The mixed-valence nature of the $NiCoMnO_4$ composites could be beneficial in energy storage applications.

Fig. 4(a) shows the XRD diffraction patterns of the as-prepared $NiCoMnO_4$ and $NiCoMnO_4$@graphene composites. All of the diffraction peaks of $NiCoMnO_4$ are well indexed to spinel $NiCo_2O_4$ (JCPDS card no. 20-0781).[26] No impurity phases are found in XRD patterns, indicating the substitution of Co by Mn could not change $NiCo_2O_4$ spinel structure. Besides the diffraction peaks of $NiCoMnO_4$, two additional small and broad diffraction peak around at 25° can be assigned to the disorderedly stacked graphene sheets.[27] No peak-shifting is observed between $NiCoMnO_4$ and $NiCoMnO_4$@graphene, suggesting graphene-wrapping does not change the crystal structure of $NiCoMnO_4$ during the calcination process. Thermogravimetric analysis (Fig. 4(b)) reveals that the mass content of graphene in composite is about 37.5 wt% in $NiCoMnO_4$@graphene composites.

3.2 Electrochemical measurements

Fig. 5 shows the rate performances of $NiCoMnO_4$ and $NiCoMnO_4$@graphene electrodes between 0.01–3 V at various current rates. Comparing to the pristine $NiCoMnO_4$, $NiCoMnO_4$@graphene delivers higher capacities especially at higher current density. As the current density increases, $NiCoMnO_4$@graphene electrodes have reversible discharge capacities of 1014.1, 975.9, 928.4, 915.4, 914.3 and 844.6 mA h g^{-1} respectively. Interestingly, when the current density reverses back to 100 mA g^{-1}, the discharge capacities of $NiCoMnO_4$@graphene recovered to the higher values (1183.8 mA h g^{-1}) than previous cycles. The increasing capacity with increasing cycles might be attributed to the electrochemical activation of active materials and the improvement of electrolyte infiltration. Such superior rate capability indicates that $NiCoMnO_4$@graphene has potential application in high-power-density lithium-ion batteries. On the contrary, the pure $NiCoMnO_4$ electrode displays a fast capacity fading along with the cycling, only retaining a discharge capacity of 33 mA h g^{-1} at 2000 mA g^{-1}. The significant improvement in rate capability of $NiCoMnO_4$@graphene should be attributed to the formation of high-conductive graphene networks in electrode, which facilitates the charge transfer and consequently reduces the polarization of the electrode. On the other hand, graphene-wrapping

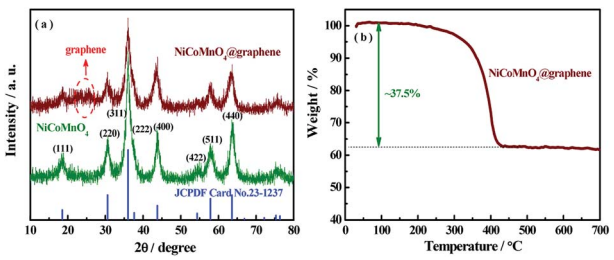

Fig. 4 (a) XRD patterns of $NiCoMnO_4$ and $NiCoMnO_4$@graphene powders. (b) TGA curves of the $NiCoMnO_4$@graphene in air atmosphere.

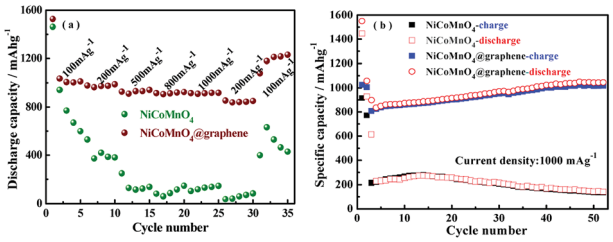

Fig. 5 (a) Rate capability and (b) cycling performances of $NiCoMnO_4$ and $NiCoMnO_4$@graphene electrodes.

could also effectively suppress aggregation of $NiCoMnO_4$ particle, reduce interfacial resistance among $NiCoMnO_4$ particles, and facilitate electron transfer in composites.

Fig. 5(b) shows the cycling behavior of $NiCoMnO_4$ and $NiCoMnO_4$@graphene electrodes at a current density of 1000 mA g^{-1} in 0.01–3.0 V. It is clear that $NiCoMnO_4$@graphene delivers a higher discharge capacity and exhibits excellent cycling stability. After 50 cycles, $NiCoMnO_4$@graphene electrode delivers a reversible capacity of 1045.1 mA h g^{-1} while $NiCoMnO_4$ electrode is merely 143.4 mA h g^{-1}. The continuous increase in capacity of $NiCoMnO_4$@graphene during the initial 50 cycles might be associated with two phenomena: (a) a gradual activation of graphene during conversion process, and (b) the improvement of electrolyte infiltration. The comparison summarized in Table 1 indicates that $NiCoMnO_4$@graphene with excellent performances could be a promising candidate for high-energy lithium-ion batteries.

A series of electrochemical measurements are performed to investigate the effect of graphene-wrapping on Li-ion kinetic behaviors in composites. Fig. 6(a) and (b) shows the cyclic voltammograms of the first six cycles for $NiCoMnO_4$ and $NiCoMnO_4$@graphene electrode in the voltage range of 0.01–3 V *vs.* Li/Li^+ at a scan rate of 0.2 mV s^{-1}, respectively. A distinct peak is observed around 0.56 V in the initial cathodic scanning for $NiCoMnO_4$ sample, which is assigned to the reduction of $NiCoMnO_4$ to Ni, Co and Mn and the formation of a solid electrolyte interface (SEI) layer.[28] In the anodic process, two broad oxidation peaks are found at 1.59 and 1.97 V, corresponding to the oxidation of Mn^0 to Mn^{2+}, Ni^0 to Ni^{2+} and Co^0 to Co^{2+}, respectively.[28,34] Based on the above CV analysis and other's reports,[28,34] the lithium insertion/extraction reactions for plum candy-like $NiCoMnO_4$ anodes are believed to be processed as follows:

$$NiCoMnO_4 + 8Li^+ + 8e^- \rightarrow Ni + Co + Mn + 4Li_2O \quad (1)$$

$$Ni + Co + Mn + 4Li_2O \leftrightarrow NiO + CoO + MnO + 6Li^+ + 6e^- \quad (2)$$

$NiCoMnO_4$@graphene electrode exhibits similar cathodic and anodic behaviors. In the following cycle, the cathodic peak gradually shifts to higher voltage range and becomes much broader, while the anodic peak keeps almost the same as the first cycle. From the second cycle onward, the CV curves overlap of $NiCoMnO_4$@graphene electrode is found to be better than

Table 1 The comparison of electrochemical performances between our work and other's reports

Materials	Current density (mA g^{-1})	Capacity (mA h g^{-1})	Reference
$NiCoMnO_4$@graphene	**1000**	**1045 after 50 cycles**	**This work**
Carbon coated Ni–Co–Mn–O	450	395 after 50 cycles	28
Ni–Co–Mn oxide TS-HS	1000	700 after 200 cycles	21
$Mn_{0.4}Ni_{0.6}Co_2O_4$ nanowires	100	786 after 175 cycles	29
$NiCo_2O_4$/G nanosheet	300	806 after 55 cycles	13
$NiCo_2O_4$@graphene	200	994 after 50 cycles	18
NiO–$MnCo_2O_4$	200	846 after 50 cycles	30
$NiCo_2O_4$@GO	100	789.9 after 100 cycles	31
Co_3O_4@graphene	1000	967 after 100 cycles	32
Co_3O_4/graphene	1000	827 after 50 cycles	33

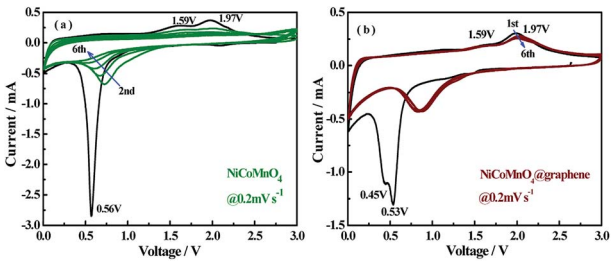

Fig. 6 CV curves of the (a) $NiCoMnO_4$ and (b) $NiCoMnO_4$@graphene electrodes at a scanning rate of 0.2 mV s^{-1}.

that of $NiCoMnO_4$ electrode, suggesting that the graphene-coating helps to enhance lithiation/delithiation reversibility and cycle stability.[18,35]

To investigate the potential mechanism behind the improved performances of $NiCoMnO_4$@graphene, electrochemical impedance spectra (EIS) of $NiCoMnO_4$ and $NiCoMnO_4$@graphene electrodes after 15, 30, 50 cycles at 1000 mA g^{-1} in the fully discharged state, are carried out, shown Fig. 7(a and b). All EIS curves are fitted with the equivalent circuits shown in Fig. 7(c), where R_s is the solution resistance, R_{SEI} stands for the resistance of the SEI film, R_{ct} was the charge transfer resistance at the particle/electrolyte interface. According to the equivalent circuit, the values of R_{ct} for the $NiCoMnO_4$ electrodes are calculated to be 110.0, 520.7 and 3010.0 Ω respectively, while the R_{ct} of $NiCoMnO_4$@graphene electrodes are only 10.0, 10.9 and 13.4 Ω. High-conductivity graphene network among $NiCoMnO_4$ particles should be responsible for the reduction in R_{ct}.[36] Moreover, it is expected that graphene-wrapping acting as a cage-like framework around $NiCoMnO_4$, efficiently suppresses aggregation of $NiCoMnO_4$ particle due to volume expansion and facilitates electron transfer in the electrode.[37]

Fig. 8 shows the morphologies of $NiCoMnO_4$ and $NiCoMnO_4$@graphene particles after 15 cycles at 1000 mA g^{-1}, respectively. Fig. 8(b) shows that $NiCoMnO_4$ particles has serious structure-deterioration and losses its plum candy-like morphologies, which would not only increase interfacial resistance among particles but also reduce the contact areas of active materials with the electrolyte. Fig. 8(c) reveals that $NiCoMnO_4$@graphene electrode has less aggregation than that (Fig. 8(a)) of the bare one, and unambiguously confirms the graphene-network in the electrode. In contrast, as shown in Fig. 8(d), $NiCoMnO_4$@graphene powders can maintain the plum candy-like structure well, further confirming that

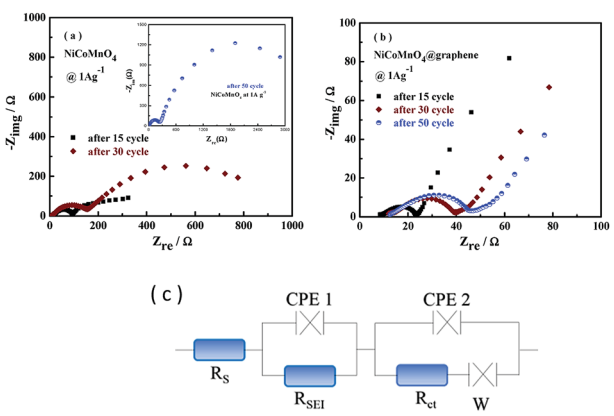

Fig. 7 (a) Electrochemical impedance spectroscopies of (a) $NiCoMnO_4$ and (b) $NiCoMnO_4$@graphene at the full discharged state after 15, 30, 50 cycles. (c) The equivalent circuit for EIS fitting.

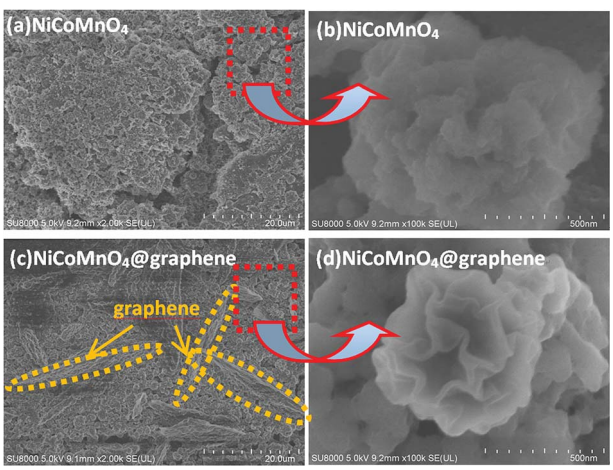

Fig. 8 FE-SEM images of (a and b) $NiCoMnO_4$ and (c and d) $NiCoMnO_4$@graphene after 15 cycles of 1000 mA g^{-1}, respectively.

graphene-wrapping indeed efficiently withstands the structural strain in $NiCoMnO_4$, enhance the structure stability during the electrochemical cycling, and consequently offer more active sites for Li-ion insertion/extraction. As a result, the electrochemical performances are enhanced.

To further study the effect of graphene-wrapping on the Li-ion diffusion kinetics of $NiCoMnO_4$, the electrochemical impedance spectra under different charge/discharge states after 15 cycles for $NiCoMnO_4$ and $NiCoMnO_4$@graphene electrodes are continuously measured during the lithium-ion insertion/extraction process. The cells are charged/discharged at 100 mA g^{-1} and the electrochemical impedance spectra are recorded for every 10 min. The EIS spectra (Z'' *vs.* Z') of $NiCoMnO_4$ and $NiCoMnO_4$@graphene electrodes are shown in Fig. 9. According to the equivalent circuit shown in Fig. 7(c), the charge transfer resistances (R_{ct}) are calculated and the dependences of R_{ct} on operation voltage for $NiCoMnO_4$ and $NiCoMnO_4$@graphene electrodes are given in Fig. 10(a and b). During the lithiation process, R_{ct} is found to decreases monotonously due to the formation of the SEI layer.[38] On the other hand, the cracked SEI layer induced by volume expansion of active materials would enlarge contact area between active material and electrolyte, leading to the decrease of the charge transfer resistance.[39] During the delithiation process, R_{ct} monotonously up to 695.0 Ω because of the restructuring of the SEI layer. In comparison, $NiCoMnO_4$@graphene electrodes show lower charge transfer resistances on a whole, suggesting that graphene-wrapping would favor charge transfer and structure stability of $NiCoMnO_4$ material during the charging/discharging process. Fig. 10(c and d) shows the SEI film resistance (R_{SEI}) as function of the cell voltage for $NiCoMnO_4$ and $NiCoMnO_4$@graphene electrodes. For $NiCoMnO_4$ shown in Fig. 10(c), R_{SEI} increases from 9.36 Ω to 32.3 Ω with decreasing of the cell voltage as a result of the electrolyte degradation.[40] During the lithiation process, the sharp increase of the R_{SEI} at the low voltage indicates the growth in thickness of the SEI as

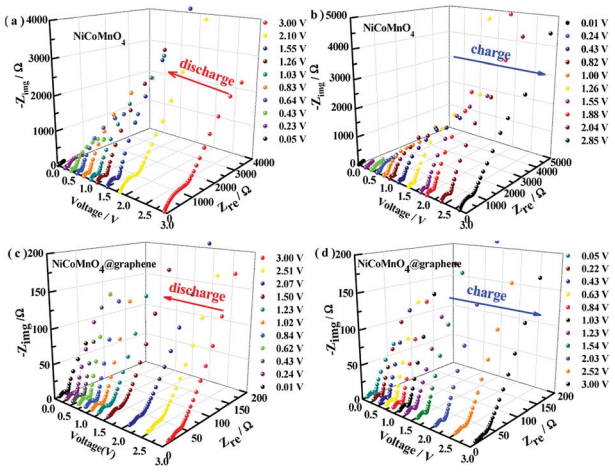

Fig. 9 The impedance spectra of $NiCoMnO_4$ and $NiCoMnO_4$@graphene electrodes under different charge/discharge states after 15 cycles of 1000 mA g^{-1}.

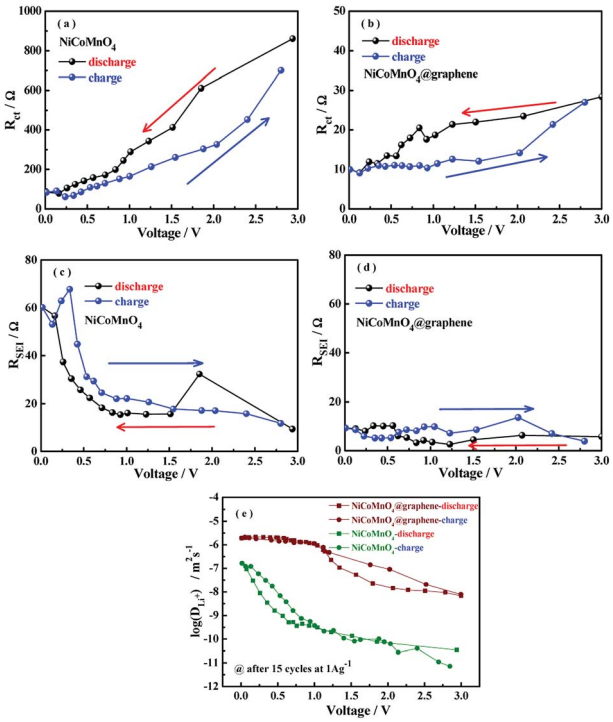

Fig. 10 (a and c) R_{SEI} and (b and d) R_{ct} at different charge/discharge states for $NiCoMnO_4$ and $NiCoMnO_4$@graphene electrodes after 15 cycles of 1000 mA g^{-1}; (e) lithium ion diffusion coefficients at different charge/discharge states for $NiCoMnO_4$ and $NiCoMnO_4$@graphene electrodes after 15 cycles of 1000 mA g^{-1}.

the potential becomes more negative.[41] During the de-alloying process, R_{SEI} decreases reversibly to the original level. Such change in R_{SEI} would be strongly related to the expansion and extraction of $NiCoMnO_4$ volume. Similar behaviors have been reported.[41,42] In contrast, $NiCoMnO_4$@graphene exhibits negligible change in R_{SEI} during the lithiation and delithiation process, indicating graphene-wrapping is helpful to the formation of stable SEI film.

The Li-ion diffusion coefficient of (D_{Li^+}) could be evaluated according to the linear relationship between the real axis (Z_{re}) and the reciprocal square root ($\omega^{-1/2}$) in the low frequency region[34]

$$Z_{re} = R_s + R_{ct} + \sigma_w \omega^{-1/2} \quad (3)$$

$$D_{Li^+} = \frac{R^2 T^2}{2n^4 F^4 \sigma_w^2 A^2 C^2} \quad (4)$$

where T, F, R and A are absolute temperature, Faraday's constant, gas constant and surface area of the electrode respectively. C is the molar concentration of Li-ion. n is the number of electrons per molecule during oxidation. σ_w was the Warburg coefficient. Fig. 10(e) shows Li-ion diffusion kinetics of $NiCoMnO_4$ and $NiCoMnO_4$@graphene during the Li-ion insertion/extraction process. Both electrodes exhibit similar Li-ion diffusion behavior. It is clear that $NiCoMnO_4$@graphene electrode exhibits larger Li-ion diffusion coefficients than those

of the pristine one, suggesting that graphene-wrapping would significantly facilitate Li-ion diffusion.

Work function is defined with respected to the Fermi energy of the electrons, reflecting the minimum kinetic energy of the electrons to overcome the barrier and escape the composite. Fig. 11(a–c) presents the surface potential images of Au foil, $NiCoMnO_4$ and $NiCoMnO_4$@graphdiyne composites, determined by Kelvin probe atomic force microscopy. Here, Au foil is served as calibration sample whose work function (Φ_{Au}) is 5.31 eV. According to our previous work,[16] the work functions of $NiCoMnO_4$ and $NiCoMnO_4$@graphdiyne are evaluated, shown in Fig. 11(d). It is found that $NiCoMnO_4$@graphdiyne has a smaller work function (5.10 eV) than that (5.20 eV) of $NiCoMnO_4$. Smaller work function reflects less energy for electrons to escape from $NiCoMnO_4$@graphdiyne, resulting from the high-conductive graphene network in composite. As a result, the electrochemical performances are correspondingly enhanced.

The energy-band model is employed to explain the reduction in work function of the composite because of the graphene-wrapping. Due to their different work functions, the free electrons would transfer from graphene with low work function to the $NiCoMnO_4$ with high work function at the interface between graphene and $NiCoMnO_4$ until the Fermi levels are aligned. Under equilibrium, the graphene is positively charged while the $NiCoMnO_4$ is negatively charged at the interface, and a Schottky electric field is consequently established.[43] Due to the low carrier-density concentration in the $NiCoMnO_4$ semiconductor, Schottky electric field could not be effectively screened and the free electrons tend to accumulate near the $NiCoMnO_4$ surface, which might be favorable for the redox activity of the $NiCoMnO_4$.[44] As a result, the electrochemical performances of $NiCoMnO_4$@graphene are significantly improved.

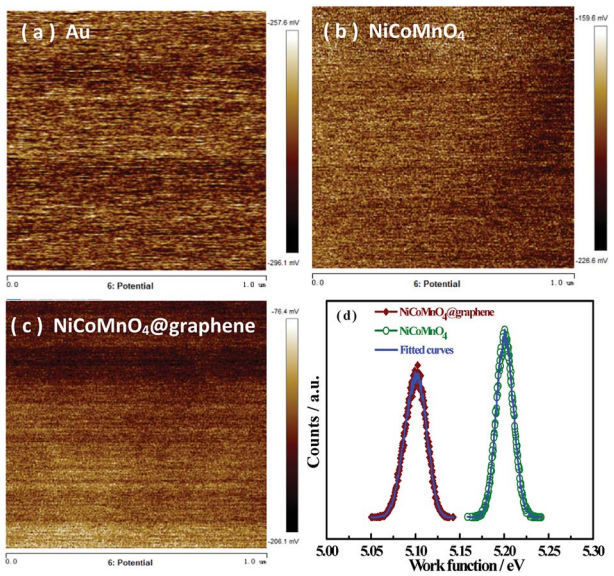

Fig. 11 Surface potential maps of (a)Au foil, (b) $NiCoMnO_4$ and (c) $NiCoMnO_4$@graphene powders; (d) work functions of $NiCoMnO_4$ and $NiCoMnO_4$@graphene composites.

4. Conclusions

3D plum candy-like $NiCoMnO_4$ microspheres have been prepared by ultrasonic spraying with the help of vacuum and subsequently wrapped by graphene through electrostatic self-assembly. $NiCoMnO_4$@graphene delivers a high reversible capacity of 844.6 mA h g^{-1} at a current density of 2000 mA g^{-1} and 1045.1 mA h g^{-1} at 1000 mA g^{-1} after 50 cycles. Such hierarchical porous structure helps to facilitate electron transfer, Li-ion kinetic diffusion in composites and accommodating the mechanical stress. In addition, high-conductive graphene network could reduce the charge-transfer resistance and enhance structural stability of $NiCoMnO_4$ materials, resulting in the significant improvement in the electrochemical performances. Moreover, Schottky electric field due to the difference in work function between graphene and $NiCoMnO_4$ might be favorable for the redox activity of the $NiCoMnO_4$.

Conflicts of interest

There are no conflicts to declare.

Acknowledgements

This work was supported by the Key Project of Department of Science & Technology of Fujian Province (No. 2014H0020) and Solar Energy Conversion & Energy Storage Engineering Technology Innovation Platform (No. 2018L3006).

References

1 J. B. Goodenough, *Energy Environ. Sci.*, 2014, **7**, 14.
2 Z. P. Cano, D. Banham, S. Ye, A. Hintennach, J. Lu, M. Fowler and Z. Chen, *Nat. Energy*, 2018, **3**, 279.
3 M. Li, J. Lu, Z. Chen and K. Amine, *Adv. Mater.*, 2018, **30**, 1.
4 N. Nitta, F. Wu, J. T. Lee and G. Yushin, *Mater. Today*, 2015, **18**, 252.
5 S. J. Lee, H. J. Kim, T. H. Hwang, S. Choi, S. H. Park, E. Deniz, D. S. Jung and J. W. Choi, *Nano Lett.*, 2017, **17**, 1870.
6 K. Zhou, L. Lai, Y. Zhen, Z. Hong, J. Guo and Z. Huang, *Chem. Eng. J.*, 2017, **316**, 137.
7 M. V. Reddy, G. V. Subba Rao and B. V. R. Chowdari, *Chem. Rev.*, 2013, **113**, 5364.
8 Y. Zhao, X. Li, B. Yan, D. Xiong, D. Li, S. Lawes and X. L. Sun, *Adv. Energy Mater.*, 2016, **6**, 1.
9 T. Jiang, F. Bu, X. Feng, I. Shakir, G. Hao and Y. Xu, *ACS Nano*, 2017, **11**, 5140.
10 M. Zheng, H. Tang, L. Li, Q. Hu, L. Zhang, H. Xue and H. Pang, *Adv. Sci.*, 2018, **5**, 1700592.
11 F. Fu, J. Li, Y. Yao, X. Qin, Y. Dou, H. Wang, J. Tsui, K. Y. Chan and M. Shao, *ACS Appl. Mater. Interfaces*, 2017, **9**, 16194.
12 Y. Wang, P. Liu, K. Zhu, J. Wang, K. Yan and J. Liu, *Electrochim. Acta*, 2018, **273**, 1.
13 Y. Chen, J. Zhu, B. Qu, B. Lu and Z. Xu, *Nano Energy*, 2014, **3**, 88.

14 J. Xu, D. Su, W. Bao, Y. Zhao, X. Xie and G. Wang, *J. Alloys Compd.*, 2016, **684**, 691.
15 C. Ding, L. Wang, W. Zhou, D. Wang, Y. Du and G. Wen, *Chem. Eng. J.*, 2018, **353**, 340.
16 W. Chen, L. Y. Wei, Z. Y. Lin, Q. Liu, Y. Chen, Y. B. Lin and Z. G. Huang, *RSC Adv.*, 2017, **7**, 47602.
17 Y. Mo, Q. Ru, X. Song, L. Guo, J. Chen, X. Hou and S. Hu, *Carbon*, 2016, **109**, 616.
18 J. Yang, H. Tian, J. Tang, T. Bai, L. Xi, S. Chen and X. Zhou, *Appl. Surf. Sci.*, 2017, **426**, 1055.
19 Y. Duan, Y. Huo, Y. Qi, L. Li, Q. Wu, C. Wang and Z. Su, *J. Alloys Compd.*, 2018, **767**, 223.
20 M. Thommes, K. Kaneko, A. V. Neimark, J. P. Olivier, F. Rodriguez-Reinoso, J. Rouquerol and K. S. W. Sing, *Pure Appl. Chem.*, 2015, **87**, 1051.
21 D. Luo, Y. P. Deng, X. Wang, G. Li, J. Wu, J. Fu, W. Lei, R. Liang, Y. Liu, Y. Ding, A. Yu and Z. Chen, *ACS Nano*, 2017, **11**, 11521.
22 J. F. Marco, J. R. Gancedo, M. Gracia, J. L. Gautier, E. Ríos and F. J. Berry, *J. Solid State Chem.*, 2000, **153**, 74.
23 R. Ding, L. Qi, M. Jia and H. Wang, *J. Power Sources*, 2014, **251**, 287.
24 Y. Mo, Q. Ru, X. Song, S. Hu, L. Guo and X. Chen, *Electrochim. Acta*, 2015, **176**, 575.
25 E. Umeshbabu and G. Ranga Rao, *Electrochim. Acta*, 2016, **213**, 717.
26 M. Liu, L. Wang, Y. Mu, J. Ma, Y. Zhao, Y. Wang, X. Lai, J. Bi and D. Gao, *Scr. Mater.*, 2018, **146**, 13.
27 Z. Wu, W. Ren, L. Wen, L. Gao, J. Zhao, Z. Chen, G. Zhou, F. Li and H. Cheng, *ACS Nano*, 2010, **4**, 3187.
28 D. McNulty, H. Geaney and C. O. Dwyer, *Sci. Rep.*, 2017, **7**, 1.
29 A. F. Shaikh, R. S. Kalubarme, M. S. Tamboli, S. S. Patil, M. V. Kulkarni, D. R. Patil, S. W. Gosavi, C. J. Park and B. B. Kale, *ChemistrySelect*, 2017, **2**, 4630.
30 T. Li, X. Li, Z. Wang, H. Guo, Q. Hu and W. Peng, *Electrochim. Acta*, 2016, **191**, 392.
31 H. Rong, Y. Qin, Z. Jiang, Z. J. Jiang and M. Liu, *J. Alloys Compd.*, 2018, **731**, 1095.
32 R. Hu, H. Zhang, Y. Bu, H. Zhang, B. Zhao and C. Yang, *Electrochim. Acta*, 2017, **228**, 241.
33 Y. Yang, J. Huang, J. Zeng, J. Xiong and J. Zhao, *ACS Appl. Mater. Interfaces*, 2017, **9**, 32801.
34 L. Wu, J. Lang, S. Wang, P. Zhang and X. Yan, *Electrochim. Acta*, 2016, **203**, 128.
35 X. Hu, G. Zeng, J. Chen, C. Lu and Z. Wen, *J. Mater. Chem. A*, 2017, **5**, 4535.
36 Z. Li, L. Zhang, X. Ge, C. Li, S. Dong, C. Wang and L. Yin, *Nano Energy*, 2017, **32**, 494.
37 Y. Gu, Z. Jiao, M. Wu, B. Luo, Y. Lei, Y. Wang, L. Wang and H. Zhang, *Nano Res.*, 2017, **10**, 121.
38 Y. Xia, Z. Xiao, X. Dou, H. Huang, X. Lu, R. Yan, Y. Gan, W. Zhu, J. Tu, W. Zhang and X. Tao, *ACS Nano*, 2013, **7**, 7083.
39 A. T. Tesfaye, Y. D. Yücel, M. K. S. Barr, L. Santinacci, F. Vacandio, F. Dumur, S. Maria, L. Monconduit and T. Djenizian, *Electrochim. Acta*, 2017, **256**, 155.
40 A. Mahmoud, M. Chamas and P. E. Lippens, *Electrochim. Acta*, 2015, **184**, 387.
41 Y. M. Lee, J. Y. Lee, H. T. Shim, J. K. Lee and J. K. Park, *J. Electrochem. Soc.*, 2017, **154**, A515.
42 S. Zhang, M. S. Ding, K. Xu, J. Allen and T. R. Jow, *Electrochem. Solid-State Lett.*, 2001, **4**, A206.
43 J. Qi, H. Zhang, D. Ji, X. Fan, L. Cheng, H. Liang, H. Li, C. Zeng and Z. Zhang, *Adv. Mater.*, 2014, **26**, 3735.
44 C. Zhang, X. P. Geng, S. L. Tang, M. S. Deng and Y. W. Du, *J. Mater. Chem. A*, 2017, **5**, 5912.